Algorithm Theoretical Basis Document

CHRIS/PROBA
Noise Reduction Module

Version 2.0, April 2008

Luis Gómez-Chova[1], Luis Alonso[1], Luis Guanter[2], Javier Calpe[1], Jose Moreno[1]

[1] *University of Valencia, Dr. Moliner 50, 46100, Burjassot–Valencia (Spain)*

[2] *GeoForschungsZentrum Potsdam, Telegrafenberg 14473, Potsdam (Germany)*

Development of CHRIS/PROBA modules for the BEAM toolbox
ESA ESRIN Contract No. 20442/07/I-LG

Contents

Abstract

This document describes the theoretical basis of the modules developed for the BEAM toolbox to reduce the noise affecting the Compact High Resolution Imaging Spectrometer (CHRIS). In addition to typical random noise, CHRIS hyperspectral images are affected by non-periodic partially deterministic disturbance patterns coming from the image formation process. The objective of the algorithms presented in this document is to correct or reduce these noise signals before any further processing.

One of the errors affecting CHRIS images is the fact that transmission of channel 2 randomly produces anomalous odd pixels in image rows (drop-outs). These errors must be identified and corrected by making use of both spatial and spectral information of the anomalous pixel and its neighbours. Another well-known problem of CHRIS images is a spatial coherent noise known as vertical striping (usually found in images acquired by push-broom sensors). This multiplicative noise in image columns comes from irregularities of the entrance slit and CCD elements in the across-track direction. Although the whole system was fully characterized after assembly, to obtain the gain correction factors that would produce an even image, the vertical pattern due to the slit is heavily dependant on the sensor temperature and thus it must be modeled and corrected.

Acronyms and Abbreviations

ATBD Algorithm Theoretical Basis Document

BEAM Basic ERS & Envisat (A)ATSR and MERIS

CCD Charge Coupled Device

CHRIS Compact High Resolution Imaging Spectrometer

ESA European Space Agency

HDF Hierarchical Data Format

LPF Low Pass Filter

LUT Look-Up Table

PROBA PRoject for On-Board Autonomy

SAD Spectral Angle Distance

SNR Signal-to-Noise Ratio

TOA Top Of Atmosphere

VS Vertical Striping

1 Introduction

Hyperspectral images acquired by remote sensing instruments are generally affected by two kinds of noise. The first one can be defined as standard random noise, which varies with time and determines the minimum image signal-to-noise ratio (SNR) (Aiazzi et al., 2002; Wettle et al., 2004). In addition, hyperspectral images can present non-periodic partially deterministic disturbance patterns (Barducci and Pippi, 2001), which come from the image formation process and are characterized by a high degree of spatial and spectral coherence (Barducci et al., 2005). This document focus on modeling and correcting the coherent spatial and spectral structures produced by these systematic disturbances.

The Compact High Resolution Imaging Spectrometer (CHRIS) Barnsley et al. (2004), which is mounted on board the European Space Agency (ESA) small satellite platform called PROBA (*Project for On Board Autonomy*) Bernaerts et al. (2000), is a push-broom imaging spectrometer. Instruments operated in a push-broom mode consist of an optical system forming a line image of the Earth onto the entrance slit of a spectrometer, and an area-array detector at the spectrometer focal plane. Usually, the detector is a charge coupled device (CCD) two dimensional array whose rows are assigned to separate wavelengths, and columns to separate resolved points in the Earth image (Mouroulis et al., 2000). Figure 1 shows the push-broom operation mode for the acquisition of spectral images. The optical system collects the light arriving from a long and narrow strip of the surface below by means of a thin slit. The system is oriented perpendicularly to the direction of motion of the sensor and the sequential acquisition of lines as the platform moves forward generates the image. The image of the strip of land is diffracted separating the different wavelengths and projected onto a properly aligned CCD array, so the line is parallel to the horizontal axis (spatial) while the diffraction is produced along the perpendicular axis (spectral).

Summarizing, the complete optical design is optimized so that monochromatic images of the slit fall on straight CCD rows, and line spectra of resolved ground areas fall on CCD columns. In this case, each pixel in a line of the image at a given wavelength has been acquired by a different element of the CCD; while every column of the image for that wavelength has been measured by the same element of the CCD. Would be the CCD and the slit ideally built then all the CCD elements would have the same sensitivity and response, producing even and noise-free images. However, in real devices, deviations from these design conditions produce undesired effects (Barducci and Pippi, 2001; Guanter et al., 2007). One of them is the variation of the intensity of an homogeneous imaged area in each column of the CCD array, which is due to sensitivity variations between neighboring elements of the CCD and variations on the width of the slit along its length (Barducci and Pippi, 2001). The effect of these imperfections in the resulting image is a vertical pattern known as '*vertical striping*' (VS).

Usually, the whole system is fully characterized after assembly, obtaining the actual gain correction factors that would produce an even image in operational situations. However, in some occasions, especially after rocket launch, the system is affected in such a way that the characterization does not remove completely the noise. Also, this type of sensors degrade with

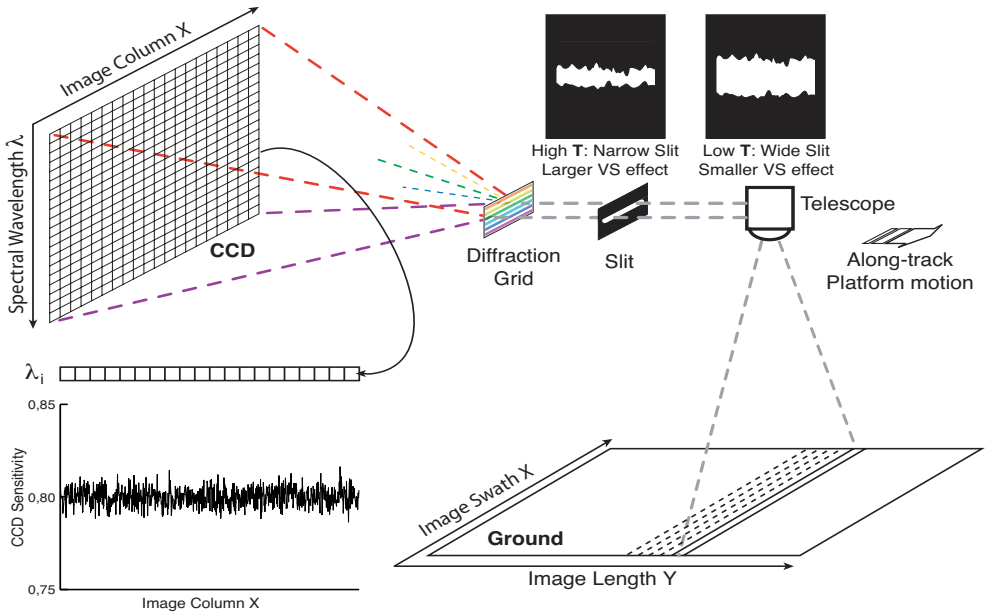

Figure 1: Design of a push-broom imaging spectrometer that shows its operation mode and the sources of the coherent spatial noise patterns: entrance slit width that depends on temperature (T), and CCD sensitivity. (Figure based on an original of *Barducci et.al.*).

time, and thus need a recalibration, which is not always possible. In those cases, a noise reduction algorithm must be applied after image reception in the pre-processing phase.

As a push-broom sensor, the radiometric response of the CHRIS instrument is determined by two overlapping components: the optical system response (a telescope forming an image onto the entrance slit of a spectrometer) and the CCD response (a thinned, back-illuminated, frame-transfer CCD) (Bernaerts et al., 2000). With regard to the CCD response, the different pixel-to-pixel response comes from non-uniformities on dark current generation, non-uniformities on pixel sensitivity, threshold variations, and gain and off-set differences (Theuwissen, 1995). But, in practice, these CCD imperfections are relatively stable with temperature and time (Cutter, 2004) resulting in a spatially fixed-pattern noise in the image that should be removed (e.g. the dark signal offsets are removed by subtracting a generic dark image). However, with regard to the optical system response, changes in temperature, due to the seasonal variation of the in-orbit CHRIS instrument temperature (Cutter, 2004), produce a dilation of the slit and changes its width and moves the image of the slit across the detector. Therefore, the effect of the slit adds up to the vertical pattern in a complex way, as it is dependent on the sensors temperature heavily (see Fig. 1), and thus it must be modeled and corrected.

In addition to this noise produced at the image formation process, the transmission of CHRIS channel 2 randomly fails producing anomalous values at the odd pixels in some image rows called '*drop-outs*'. Drop-outs hamper the operational use of CHRIS images since later processing stages are drastically affected by these anomalous pixels. These errors must be corrected by making use of both spatial and spectral information of the anomalous pixel and its neighbours.

In this document, we focus on modeling and correcting the coherent spatial and spectral noise patterns produced by these systematic, yet hardly predictable, disturbances. The document describes in detail the drop-out and vertical striping correction algorithms, which are implemented in the BEAM software, supported by ESA, for the pre-processing of CHRIS/PROBA data.

2 Hyperspectral Data-cube

A hyperspectral image consists of two spatial dimensions (along-track and across-track) and one spectral dimension (wavelength). This hyperspectral image is registered by the instrument in a data-cube where: the along-track dimension at the Earth surface, y, corresponds to the image-lines dimension l (distributed in the vertical direction of the image); the surface across-track dimension, x, corresponds to the line-pixels dimension p (distributed in the horizontal direction of the image and CCD); and the spectral dimension, λ, corresponds to the image band b (distributed in the vertical direction of the CCD). These correspondences among Earth surface, instrument CCD, and hyperspectral data-cube are depicted in Fig. 2. The size of the hyperspectral data-cube can be written in the form $N_l \times N_p \times N_b$, where N_l is the number of image lines, N_p is the number of pixels per line, and N_b is the number of spectral bands. The incoming radiance is integrated over the spatial and spectral response of the system for a given detector element (p, b) of the CCD array. The relation between the incoming *at sensor* radiance from the Earth surface, $L(x, y, \lambda)$ (W m^{-2} sr^{-1} nm^{-1}), and the registered value by the CCD, $I(l, p, b)$ (*digital number*), can be defined as:

$$I(l,p,b) = S(p,b)\int_{y\in l}\int_{x\in p}\int_{\lambda\in b} L(y,x,\lambda)H(x,\lambda)dydxd\lambda + S_0(l,p,b) \tag{2.1}$$

where $H(x, \lambda)$ represents the optical system response, $S(p, b)$ is the CCD sensitivity, and $S_0(l, p, b)$ contains all the analog offset errors and random noise. In this equation, it is worth noting that the vertical dimension of the image is related to the time when the image line, l, was acquired. In addition, the image values, I, and CCD sensitivity, S, are expressed as a function of the image pixels and bands, (p, b). Hence, we assume a one-to-one correspondence between the image pixels and bands and the CCD columns and rows, respectively. However, usually a certain number of CCD columns or rows are binned to form the final image (e.g. reducing the spatial or spectral resolution to increase the radiometric accuracy). In this case, some lines and columns of $I(l, p, b)$ would be summed, but all the presented formulation is still valid.

If the instrument works correctly (Mouroulis et al., 2000), the spatial and the spectral dimensions (orthogonal dimensions of the CCD), are independent and they can be processed separately. Therefore, the optical system response can be expressed as $H(x, \lambda) = H(x)H(\lambda)$, where $H(x)$ corresponds to the slit response and $H(\lambda)$ corresponds to the instrument chromatic response, which in turns defines the wavelength and bandwidth of each band. Thus, the slit response is constant for all the lines and bands of a given image, and independent from pixel-to-pixel.

Assuming a smooth optical response, the integral of the incoming radiance over the optical response of the system in Eq. (2.1), which represents the radiance at the focal plane array of the

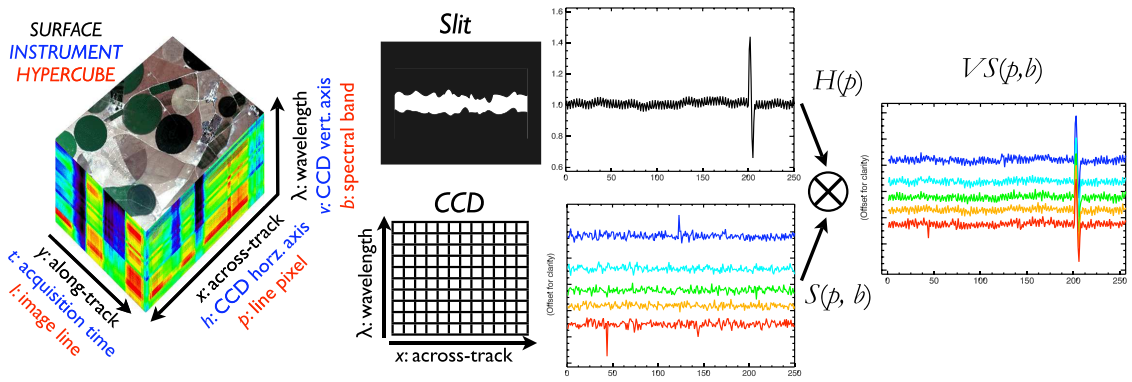

Figure 2: Formation process of the vertical striping, $\nu(p,b)$, from the combination of the non-uniform CCD pixel response, $S(p,b)$, and the slit optical response, $H_x(p)$, which are constant in columns.

CCD, can be approximated as:

$$\int_{y\in l}\int_{x\in p}\int_{\lambda\in b} L(y,x,\lambda)H(x)H(\lambda)dydxd\lambda = L(l,p,b)H_x(p)H_\lambda(b) \tag{2.2}$$

where $H_x(p)$ and $H_\lambda(b)$ represent the contribution of the spatial and spectral response to the calibration coefficient of the detector element (p,b). Then, the relation between the incoming radiance and the registered value by the CCD of Eq. (2.1) can be written as:

$$I(l,p,b) = L(l,p,b)H_x(p)H_\lambda(b)S(p,b) + S_0(l,p,b) \tag{2.3}$$

Most of existing CCD sensors allow an accurate correction of dark current offsets, thus making $S_0(l,p,b)$ negligible, i.e. remaining only random noise of zero mean and low amplitude). In addition, the provided CHRIS level 1a images are radiometrically corrected (so the units of I are radiance units instead of digital numbers). Version 4.1 of CHRIS products[1] are processed using an improved radiometric calibration which was poor in previous versions (underestimation up to a factor two of the sensor measurements in the NIR). Cutter (2004) and Guanter et al. (2005) showed that CHRIS images present an accurate spectral-radiometric calibration that allows us to remove the dependency with the spectral response $H_\lambda(b)$. Hence, assuming that $S_0(l,p,b) \simeq 0$ and $H_\lambda(b) \simeq 1$, Eq. (2.3) is reduced to:

$$I(l,p,b) = L(l,p,b)H(p)S(p,b) = L(l,p,b)\nu(p,b) \tag{2.4}$$

where the vertical striping produced by the combination of the two non-uniform spatial responses is denoted by $\nu(p,b)$. A spectral band b will be acquired by the same row of CCD elements, and each image column p will be affected by a different CCD pixel response $S(p,b)$ and a different optical slit response $H(p)$ (equal for all spectral bands). Therefore, the resulting multiplicative

[1]CHRIS products are provided in *top of the atmosphere* radiance in a HDF v4 file format, which includes additional acquisition information (image date, azimuth and zenith view angles, etc) contained in the metadata attributes of the CHRIS HDF file (Cutter and Johns, 2005b).

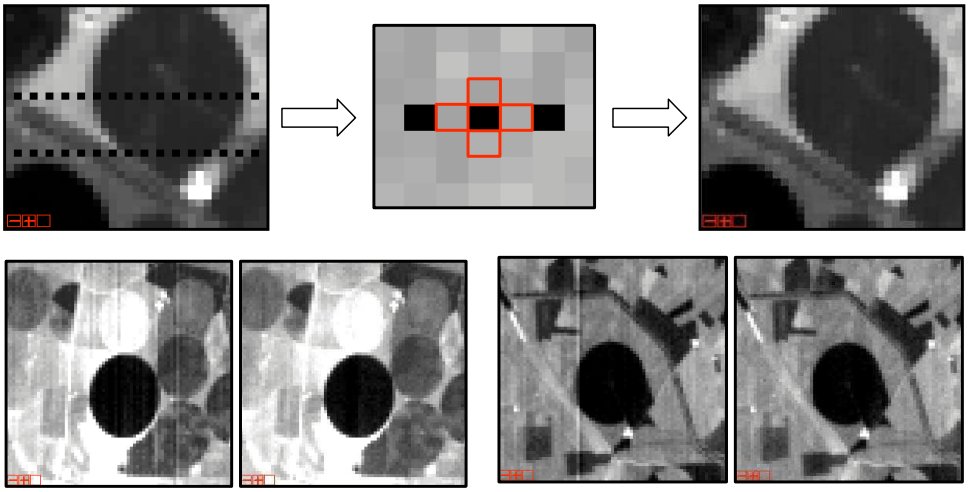

Figure 3: Illustration of a correction of the drop-out errors based on the four-connected neighbours (*top*) and the vertical striping (*bottom*). Credits: Garcia and Moreno (2004).

noise $\nu(p, b)$ is constant in image columns and superimposes a systematic pattern of noise organized by vertical lines. The formation of the stripe noise is depicted in Fig. 2.

The physical interpretation of satellite data needs an accurate sensor characterization that corrects the provided (radiometrically calibrated) product, $I(l, p, b)$, in order to obtain values as close as possible to the desired at-sensor radiance, $L(l, p, b)$. Therefore, the procedure consists in finding the set of correction coefficients, which characterize the vertical striping $\nu(p, b)$, to retrieve the true radiance $L(l, p, b) = I(l, p, b)/\nu(p, b)$.

3 Drop-out Correction

The process of estimating and correcting vertical striping patterns directly from the image is drastically affected by drop-out errors since these pixels present anomalous values (usually negative) in some bands. Figure 3 shows an example of the effects of both types of noises and the images after the correction. Therefore, before vertical striping correction could be carried out, drop-out errors must be corrected in order to use all the lines of the image. For this reason, version 4.1 of the CHRIS data HDF file Cutter and Johns (2005a) includes a quality mask that indicates pixel saturation and occurrence of errors: useful pixels, drop-out pixel (Ch2 reset), and saturated pixel. The problem is that the mask of invalid pixels is not available for versions previous to v4.1 and, in addition, this mask sometimes fails to mark drop-out pixels. In consequence, the developed correction algorithm must also detect automatically image drop-outs.

3.1 Drop-out Detection

From version release 4.1, CHRIS data includes an image quality mask, which has the same dimensions in terms of number of pixels than the CHRIS image of the HDF file, that is, a data-cube $M(l, p, b)$ of size $N_l \times N_p \times N_b$. In this mask, each pixel has one of three possible values indicating the usability of the pixel with the following meaning:

- 0: This pixel is a useful image pixel.
- 1: This pixel is a channel 2 reset pixel and holds no valuable data (Drop Out).
- 2: This pixel has saturated and holds no valuable data (Saturation).

Depending on the processing version of the CHRIS product we can have two different situations:

- If the mask is available, it has the same dimensions, in terms of number of pixels, as the CHRIS image of the HDF file. Therefore, when reading the mask from the HDF Scientific Data Set we have to perform the same corrections as for the CHRIS image:
  - Correct for backscanning of images 2 and 4 ($+36^o$ and -36^o): These images are bottom-up oriented and shall be flipped vertically in order to equally align all images.
  - Remove calibration and padding pixels: Blank Pixels (preceding and trailing) should all be removed also in the mask.
- If the mask is not available (versions previous to v4.1) we have to create an empty mask of the same size than the image and find rows with drop-out.

However, although we have the mask with the drop-outs (channel 2 reset), in some images there may be also invalid pixels that are not masked. The problem with the non-masked pixels is that they do not present negative values (their values are in the order of magnitude of the signal) but they always occur in odd columns. Therefore, whether the mask with the drop-outs is available or not, we need to improve/create the mask adding undetected drop-outs.

The anomalous pixels (drop-outs) are found as follows:

1. We assume that the difference between contiguous pixels in a row is small. The difference between a correct pixel with its neighbour should be equal or smaller than with the pixel of two columns away, except in the case that the neighbour is a drop-out. This assumption should be true for all the odd pixels of the row.
   - Square difference of odd pixels, which may be drop-outs, with neighboring even pixels that are certainly correct:

$$D_{all}(l, b) = (I(l, p, b) - I(l, p + 1, b))^2 \quad p = 1, 2, \ldots, N_p - 1 \tag{3.1}$$

   where high differences are expected in presence of drop-outs.

- Square difference of even pixels, which are certainly correct, with the following even pixel:

$$D_{even}(l,b) = (I(l,p,b) - I(l,p+2,b))^2 \quad p = 2,4,\ldots,N_p - 2 \tag{3.2}$$

  where low differences are expected in all cases (depending on the surface changes in the across-track direction).

2. Surface and vertical striping affect differences between contiguous columns, thus the 'median' is used to obtain a robust estimator of the average difference between pixels for the whole line.

3. Finally, all odd pixels of the line are labeled as drop-out noise if the difference between neighbours is 50% higher than between even pixels:

$$\begin{array}{ll} \text{IF} & \frac{\text{median}(D_{all}(l,b))}{\text{median}(D_{even}(l,b))} > 1.5 \\ \text{THEN} & M(l,p,b) = 1 \quad p = 1,3,\ldots,N_p \end{array} \tag{3.3}$$

3.2 Drop-out Restoration

Once the drop-out errors have been detected, they must be corrected by the use of both spatial and spectral information of the anomalous pixel and its neighbours. Each invalid pixel value is replaced by a weighted average of the values of the neighbouring pixels. In order to avoid the poor performance of spatial filters (local average) in border or inhomogeneous areas (Larsen et al., 1997; Garcia and Moreno, 2004), the contribution of each pixel (i,j) of a given neighbourhood (C) of size 3×3, is weighted by its similarity to the corrected pixel, $I(l,p,b)$. In particular, this similarity weight is the inverse of the Euclidean distance between the spectral signature of the pixels, which is calculated locally using the n_b upper and bottom spectral bands closer to the corrected band b:

$$\begin{array}{rcl} W(i,j) & = & \left(\sum_k (I(l,p,b) - I(l+i,p+j,b+k))^2\right)^{-1/2} \\ & & k = -n_b,\ldots,-1,1,\ldots,n_b \end{array} \tag{3.4}$$

The final weight matrix, W_C is modified to have zero values for the pixels not belonging to the given neighbourhood C and it is normalized in order to sum to one, i.e. , $W_C(i,j) = C(i,j)W(i,j)/\sum_{i,j} C(i,j)W(i,j)$. Finally, the new value of the drop-out is calculated as:

$$I(l,p,b) = \sum_{i,j} I(l+i,p+j,b)W_C(i,j) \qquad i,j = -1,0,1 \tag{3.5}$$

The result of this process is similar to a spatial interpolation but taking into account the similarity with neighbours. It is worth noting that the values of bands with errors (indicated by the CHRIS quality mask) are not considered during this process.

The correction of the drop-out errors can be carried out independently of the vertical striping correction. However, the vertical striping noise introduces different multiplicative factors in image columns that can affect the new pixel value if the local average is performed by using contiguous

columns. Therefore, if one performs the drop-out correction before the vertical striping correction, only the values of the vertical neighbours (C_2) must be used in order to avoid the effect of vertical striping:

$$C_2 = \begin{pmatrix} 0 & 1 & 0 \\ 0 & 0 & 0 \\ 0 & 1 & 0 \end{pmatrix} \tag{3.6}$$

After the vertical striping removal, it is possible to perform a second correction based on the four-connected (C_4) or eight-connected (C_8) neighbours:

$$C_4 = \begin{pmatrix} 0 & 1 & 0 \\ 1 & 0 & 1 \\ 0 & 1 & 0 \end{pmatrix} \qquad C_8 = \begin{pmatrix} 1 & 1 & 1 \\ 1 & 0 & 1 \\ 1 & 1 & 1 \end{pmatrix} \tag{3.7}$$

After the correction of the drop-out errors, a new flag should be added to the header to reflect the level of drop-out correction applied: none, first pass (vertical neighbours), or second pass (all neighbours).

4 Vertical Striping Correction

The objective of vertical striping correction methods is to estimate the correction factor, $\nu(p,b) = H(p)S(p,b)$, of each spectral band to correct all the lines of this band. The main assumption consists in considering that both slit (H) and CCD (S) contributions change from one pixel to another (high spatial frequency) in the across-track direction (p) but are constant in the along-track direction (l), i.e. during the image formation; while surface contribution (L) presents smoother profiles (lower spatial frequencies) in the across-track dimension.

4.1 Vertical striping correction methods

In the literature, all the vertical striping reduction approaches take advantage of the constant noise factors in the image columns (Barducci and Pippi, 2001; Garcia and Moreno, 2004; Settle and Cutter, 2005; Mlsna and Becker, 2006). Basically, the image is averaged in lines (along-track) and then the noise profile is estimated in the across-track direction for each band. By averaging image lines (*integrated line profile*) the surface contribution is smoothed, the additive random noise is cancelled, and the VS profile remains constant. Consequently, the surface contribution presents lower spatial frequencies in the integrated line profile and can be easily separated from the VS (high frequencies) applying a filter with a suited cut-off frequency.

Figure 4a shows the three steps of the method proposed in Barducci and Pippi (2001):

A. Each band is averaged in lines (along-track direction) obtaining one integrated line profile per band: $\alpha(p,b) = \int_1^{N_l} I(l,p,b)dl = \nu(p,b)\int_1^{N_l} L(l,p,b)dl = \nu(p,b)\beta(p,b)$.

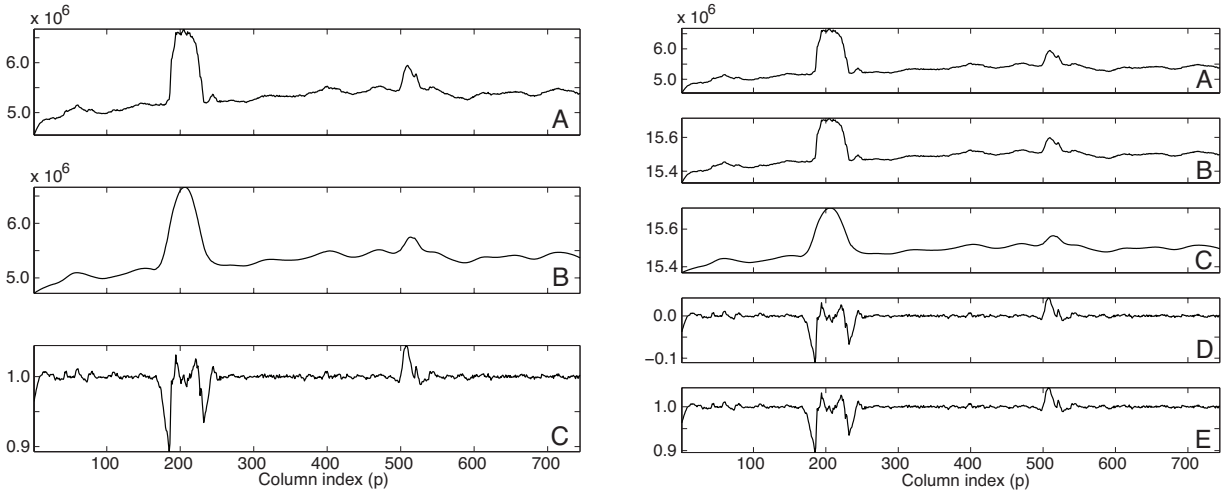

(a) (b)

Figure 4: Example of the processing steps of two different vertical striping reduction methods proposed in the literature by (a) Barducci and Pippi (2001) and (b) Settle and Cutter (2005) (profiles of the last band of CHRIS_EI_060130_63A1_41 image taken over Heron Island).

B. A low pass filter (LPF) is applied using a moving-window algorithm that flattens the profile $\alpha(p,b)$ by convolving it with a Gaussian weighting function w: $\hat{\beta}(p,b) = \text{LPF}\{\alpha(p,b)\} = \int w(p-k)\alpha(p,b)dk$. In this kind of filter, the cut-off frequency f_c defines the standard deviation of the Gaussian window, $\sigma \sim 1/f_c$.

C. Since $\hat{\beta}(p,b)$ mainly contains the surface contribution, the shape of the VS factors can be obtained by the ratio $\hat{\nu}(p,b) = \alpha(p,b)/\hat{\beta}(p,b)$. Thus, the corrected image is calculated as $\hat{L}(l,p,b) = I(l,p,b)/\hat{\nu}(p,b)$.

Figure 4b shows the method that is used by SIRA Technology Ltd. to correct CHRIS images (Settle and Cutter, 2005). The main difference with the previous method is the use of logarithms to transform the multiplicative noise into additive noise in order to improve the filtering as follows:

A. Each band is averaged in lines obtaining one integrated line profile per band, $\alpha(p,b)$.

B. Log-transform the averaged profile: $\log_\alpha(p,b) \equiv \log(\alpha(p,b)) = \log(\nu(p,b)) + \log(\beta(p,b))$

C. Applying a low pass filter in order to eliminate high frequency variations (coming from the noise ν) and estimate surface contribution: $\hat{\log}_\beta(p,b) = \text{LPF}\{\log_\alpha(p,b)\}$.

D. Obtaining high frequency variations (considered as the noise): $\hat{\log}_\nu(p,b) = \log_\alpha(p,b) - \hat{\log}_\beta(p,b)$

E. The vertical striping factors are obtained calculating the inverse of the logarithm $\hat{\nu}(p,b) = \exp(\hat{\log}_\nu(p,b))$.

Theoretically, the first approach should give poor results when filtering the line profile because it is affected by a multiplicative noise and this is equivalent to a convolution in the frequency domain. This is the main reason to propose the second approach but, in practice, both approaches give equivalent results. This can be explained because features of the multiplicative noise, which present a mean close to one ($f = 0$ and $A = 1$) and high frequency components of low amplitude ($\uparrow f$ and $A \simeq 0.1$). Therefore, when performing the convolution of the signal and noise in the frequency domain, the power spectral density of the signal at low frequencies is not affected. Since both methods provide equivalent results, we consider them as a single method and hereafter we refer to them as the *standard method*.

The standard method can fail for several reasons, such as high amplitude changes in the VS, which affect the performance of the low pass filter (wrong estimation of the surface contribution) producing an overestimation or underestimation in the correction factors of the neighboring columns. In Garcia and Moreno (2004) an iterative method that corrects the effect of these high striping values is presented. However, as proposed in the next section, these effects can be also avoided using more advanced filtering techniques that use a weight function.

4.2 Robust vertical striping correction method

One of the main drawbacks of the methods proposed in the literature is the fact that they do not take into account the possible high frequency components of the surface explicitly. In images presenting structures or patterns in the vertical direction, the averaged profile $\alpha(p, b)$ may present high frequency contributions due to the surface. This will be interpreted as vertical striping when estimating $\nu(p, b)$ (see the selected example in Fig. 4), and some columns will be corrected with wrong values, worsening the final image.

The proposed correction method is also based on the hypothesis that the vertical disturbance presents higher spatial frequencies than the surface radiance. However, it models the noise pattern by suppressing the surface contribution in the across-track in two different ways: first, avoiding the high frequency changes due to surface edges, and then subtracting the low frequency profile.

The surface can present high spatial frequencies due to: the surface texture, which has low amplitude changes; or changes in the land-cover type, which can produce great changes in amplitude being a problem in the destriping process. In principle, in one spectral band, both the surface and noise contributions are mixed and is not possible to distinguish which of them causes the changes in the radiance amplitude between contiguous columns. However, the spectral signature of pixels from current hyperspectral sensors can provide helpful information about the land cover changes. Considering the spectra of two contiguous pixels, p_1 and p_2, just in the boundary between two land-cover types, there are three factors affecting the spectral change: (*i*) differences between the true spectra of both surfaces (in shape and magnitude); (*ii*) the different CCD sensitivity $S(p, b)$, which modulates the spectral signature as a multiplicative noise of low variance; and (*iii*) the different multiplicative factor due to the slit $H(p)$, which scales the magnitude of the whole spectral signature. Among these three factors, the first one will produce the greater change, the

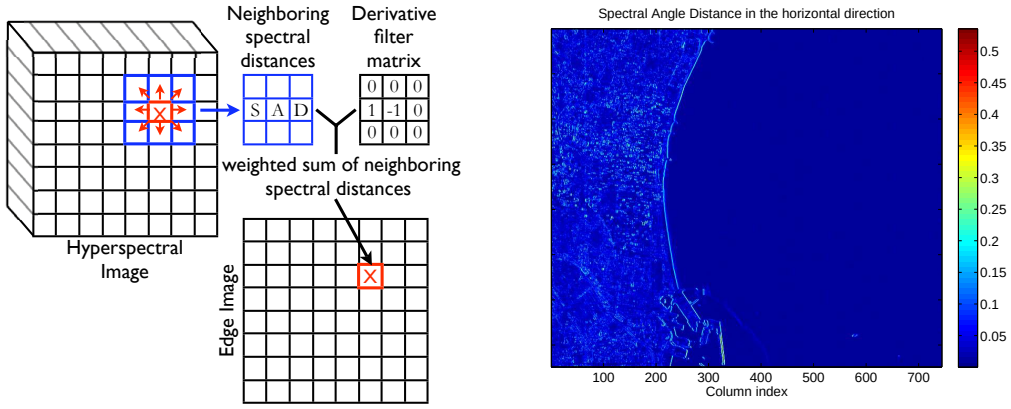

Figure 5: Approach followed to find edges in the hyperspectral image using a spatio-spectral derivative filter in the horizontal direction (Image CHRIS_PC_050518_540B_41 acquired over the port of Valencia.

second one will be a second-order factor when comparing the spectral similarity, and the third one will not affect the final result if the selected spectral distance is invariant to scaling by a positive factor. Therefore, we can apply a filter in the across-track direction of the hyperspectral image in order to find the surface borders that introduce high frequencies in the across-track profile. The next sections explain how pixels corresponding to borders are not employed when computing the integrated line profiles.

4.2.1 Spatio-Spectral Edge Detection.

We propose a spatio-spectral filter based on two-dimensional convolution filters, which are commonly used in grayscale image processing, like the *Derivation filter* and the *Roberts operator* (Pratt, 2001). In the proposed algorithm, the horizontal edge pixels of the processed hyperspectral image are found using the derivative filter in the horizontal direction $K = \left(\begin{smallmatrix} 1 & -1 \\ 0 & 0 \end{smallmatrix}\right)$. To apply these techniques to hyperspectral images, taking into account the spectral dimension, it is not possible to directly compute the convolution of the kernel matrix and the three-dimensional hypercube. In our proposal, a spectral distance is first computed between the spectrum of the pixel linked to the position with value $K(i,j) = -1$ in the kernel matrix (reference pixel), and the rest of neighboring pixels (forming a matrix D of distances with value $D(i,j) = 0$ for the reference pixel). Then, the sum of the product of the elements of the kernel and the distance matrix is computed, $\sum_{i,j} K(i,j)D(i,j)$, and the resulting value is assigned to the reference pixel (i,j). The main difference of this method compared to the case of grayscale image processing is that only one position of K can present the value -1, which indicates at each moment the pixel that is being used as a reference to compute the spectral distances. When this process is completed for all the pixels of the hyperspectral image, a sensitivity threshold must be specified, being identified as edges all pixels with values greater than this threshold, i.e. where neighbouring pixels present a different spectral signature.

Figure 5 shows the approach followed to find the edge values in the processed hyperspectral

images. Concerning the spectral distance, the Spectral Angle Distance (SAD) is used since it is invariant to multiplicative scaling (Keshava, 2004), without being affected by the vertical striping of the slit:

$$SAD(\vec{x}_1(\lambda), \vec{x}_2(\lambda)) = \arccos\left(\langle \vec{x}_1, \vec{x}_2 \rangle / (\|\vec{x}_1\| \|\vec{x}_2\|)\right), \tag{4.1}$$

where $\vec{x}_1$ and $\vec{x}_2$ are the vectors containing the spectral signature of the pixels whose spectral distance is being calculated, $\langle \cdot, \cdot \rangle$ is the dot product operator, and $\| \cdot \|$ is the quadratic norm. Finally, to make the threshold adaptable to each image, but assuring a significant number of lines to compute the smoothed integrated line profiles, an iterative procedure is followed. This procedure starts from threshold zero and iteratively increase it until finding the threshold that ensures an 80% of non-edge pixels in the column that presents more edge pixels:

$$\begin{array}{ll} \text{IF} & \sum_{i,j} K(i,j) SAD(\vec{x}(l,p), \vec{x}(l+i, p+j)) > threshold \\ \text{THEN} & Edge(l,p) = 1 \end{array} \tag{4.2}$$

4.2.2 Vertical Striping Removal.

A critical point of the proposed approach is how to remove edge pixels when computing the integrated line profiles. If all image lines that present at least one edge pixel are removed, it is probable that only few or even none of the lines can be used in the averaging. On the other hand, if the edge pixels are removed and only the remaining pixels of the line are used for averaging, then the problem is not solved since the high frequencies are still there (think in a step profile where only one point is removed). The only way to remove the edges is to work in the across-track spatial derivative domain, where the homogeneous areas before and after the edge present values close to zero and the spikes of edge pixels can be substituted interpolating prior to the integration in the along-track direction. In this simple way, all high frequency contribution by the surface is removed from the integrated line profile before the low pass filtering, and then the estimated VS is independent of the surface patterns.

Figure 6 shows the steps of the proposed method:

A. To apply logarithms in order to transform multiplicative noise in additive noise ($\log(I(l,p,b))$).

B. To transform the hyperspectral data-cube into the across-track spatial derivative domain: $\theta(l,p,b) = \frac{\partial}{\partial p} \log(I(l,p,b)) = \log(I(l,p,b)) - \log(I(l,p-1,b))$, for $p > 1$ (note that the first column derivative is fixed to zero, $\theta(l,1,b) = 0$), which is equivalent to high-pass filtering.

C. The lines of each band are averaged in the along-track direction but avoiding the edge pixels found with the spatio-spectral edge detection: $\xi(p,b) = \int_1^{N_l} \theta(l,p,b) dl$. To work in the derivative domain has allowed our method to avoid edge pixels, and it also leads to elevate the noise level temporarily because the surface power spectrum is concentrated in the low frequency region, whereas the vertical striping is spread all-over the spatial frequency spectrum (Othman and Qian, 2006). Nevertheless, if the LPF is applied in the derivative domain, the committed errors by the LPF will accumulate throughout the integration in

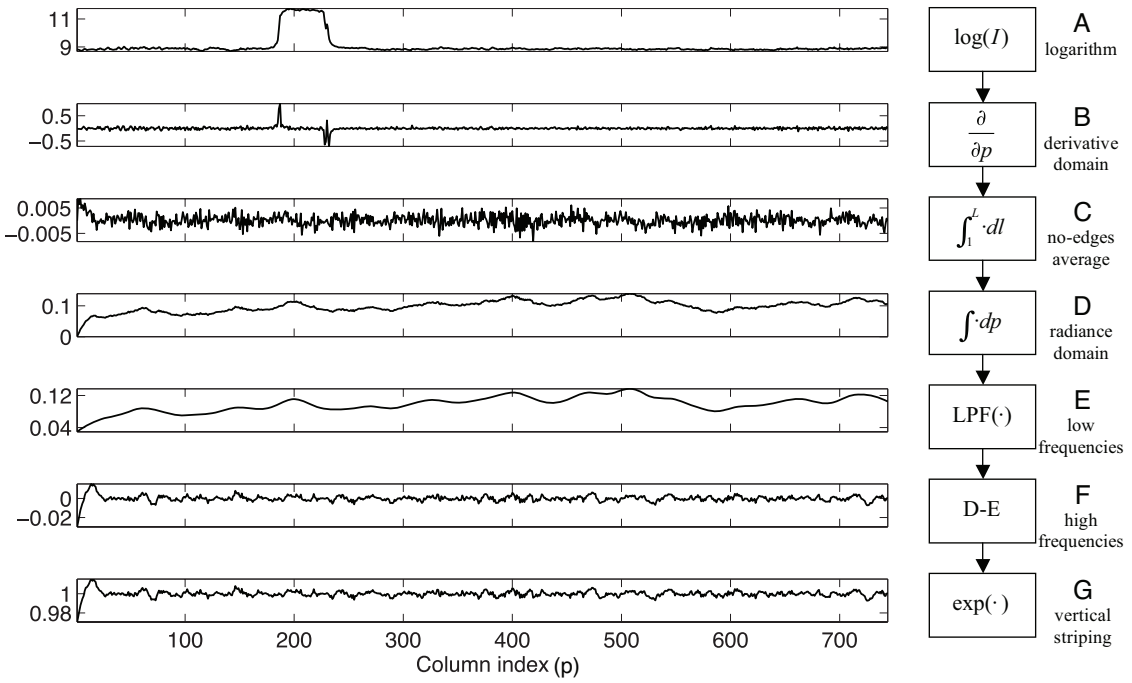

Figure 6: Example of the processing steps of proposed vertical striping correction method (profiles of the last band of CHRIS_EI_060130_63A1_41 image taken over Heron Island).

the across-track direction. Therefore, after applying the along-track LPF, data is integrated across-track to retrieve the signal in the radiance domain.

D. Integration in the across-track direction (cumulative sum in p): $\phi(p,b) = \sum_{i=1}^{p} \xi(i,b)$, i.e. the integration bias is corrected at the end of the process.

E. To apply a LPF in the across-track direction in order to eliminate the high frequency variations coming from the noise ν and estimate the surface contribution: $\varphi(p,b) = \mathrm{LPF}\{\phi(p,b)\}$.

F. To obtain the high frequency variations (considered to be the noise) by subtracting the low frequencies: $\psi(p,b) = \phi(p,b) - \varphi(p,b)$. The error committed during the integration process consists in a constant value for each band. Nevertheless, as the vertical striping is corrected independently for each band, the vertical striping in the logarithmic domain should present zero mean (gain close to 1 in the radiance image). Therefore, the offset errors are corrected subtracting the mean value: $\psi(p,b) = \psi(p,b) - 1/N_p \sum_p \psi(p,b)$.

G. Finally, the VS factors are obtained calculating the inverse of the logarithm $\hat{\nu}(p,b) = \exp(\psi(p,b))$.

4.2.3 Multiangular Vertical Striping Removal.

Thanks to the sequential acquisition of CHRIS of the same scene from five different angles, we can also improve the robustness of the proposed algorithm using together all the multiangular

images of one acquisition. As mentioned before, the VS due to the instrument slit is temperature-dependent. Although temperature recorded for different acquisitions has shown differences higher than 8°C, within a single acquisition (5 multi-angular images) the changes are less than 0.5°C. Therefore, images of one acquisition present the same vertical striping pattern while they are recording the same Earth area with different spatial patterns (slightly distorted scenes). One can take advantage of this fact to improve the estimation of the vertical striping by considering the five images as a single hyperspectral image, which is formed by stacking the multiangular images in the along-track direction, i.e. an hyper-cube with the same number of columns N_p and bands N_b, but with $5 \times N_l$ lines. When processing together a higher number of lines, the surface contribution is smoother and the estimation of the VS is more accurate.

4.3 Vertical Striping Characterization and Correction of the Slit Effect

Finally, a result of great value is the characterization of the vertical striping and its dependence on temperature. With this purpose, we corrected a significant number of CHRIS images of the database obtaining an estimation of the vertical striping pattern, $\hat{\nu}(p,b) = H(p)S(p,b)$, per image. The sensitivity of the CCD array, $S(p,b)$, is assumed to be characterized by a Gaussian distribution with unit mean. However, by applying the logarithmic transformation to the estimated VS, the multiplicative nature of both terms is changed to additive one, $\log(\hat{\nu}(p,b)) = \log(H(p)) + \log(S(p,b))$, where the term $\log(S(p,b))$ can be safely considered additive noise with zero mean distribution. As a consequence, the VS profile due to the slit, which is constant in columns, can be obtained by averaging in the spectral direction of the CCD and then reverting the logarithm: $H(p) = \exp(\int_1^{N_b} \log(\hat{\nu}(p,b))db)$. Moreover, the slit-VS profiles of the five angular images can be averaged to obtain only one $H(p)$ per acquisition, which will be associated to the platform temperature for this given acquisition: $H(p,T)$. Changes in temperature produce a dilation of the slit and changes its width and moves the image of the slit across the detector. These two effects produce a scaling of the slit-VS factors and a shift of its shape in the across-track direction, respectively, thus producing a temperature dependent vertical striping. Figure 7, on the left side, shows a peak of the obtained $H(p)$ profiles for all the analyzed Mode 2 acquisitions (Mode 2 is shown because it is not binned and presents higher across-track resolution than Mode 1). The '$*$' symbols represent the actual $H(p)$ values for each pixel column p, and the curves (continuous lines) are the corresponding spline interpolations in the across-track direction x, which provide a continuous subpixel resolution model of the striping $H(x)$ for each measured temperature T: $H(x,T)$. The curves clearly show the shift and scaling of the VS amplitude with temperature. Taking as reference the VS at $T_0 = 5.5$°C, we compute the shift in the across-track looking for the lag, $\Delta_x(T)$, of the maximum of the cross-correlation sequence between the analyzed vertical striping, $H(x,T)$, and the reference one, $H(x,T_0)$. Once the shift is corrected, the scaling factor $G_H(T)$ is computed as the slope of the linear regression that better fits $H(x,T)$ with $H(x,T_0)$ in a least-squares sense. In the central and right plots of Fig. 7 we represent the shift $\Delta_x(T)$ and scale $G_H(T)$ of the slit-VS as a function of temperature, respectively.

The estimated $\Delta_x(T)$ and $G_H(T)$ values are used to compensate the shift and scale of the

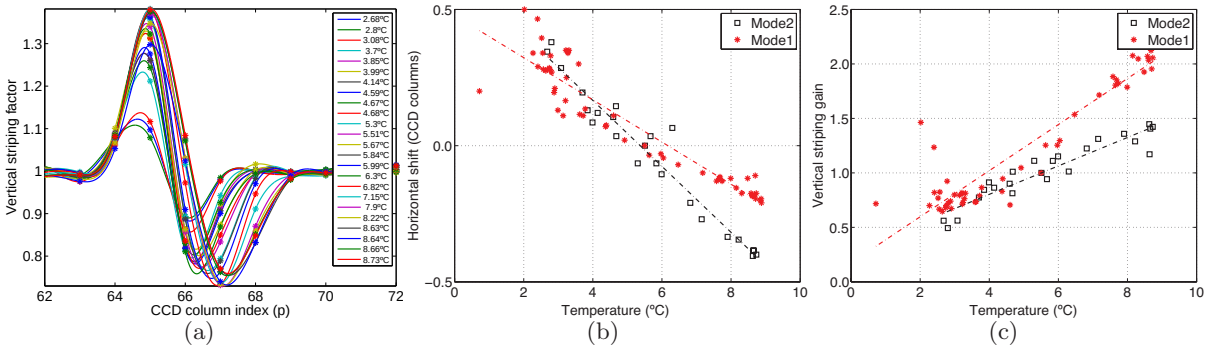

(a) (b) (c)

Figure 7: Dependence of CHRIS slit vertical striping on temperature. From left to right: (a) detail of the slit-VS profiles for all the Mode 2 acquisitions of the database ($H(p,T)$ and $H(x,T)$); (b) across-track shift of the slit-VS shape as a function of temperature ($\Delta_x(T)$); (c) scaling of the slit-VS factors as a function of temperature ($G_H(T)$).

slit-VS $H(x,T)$ and obtain the corresponding slit-VS for each acquisition of the database, but expressed at the reference temperature T_0. The average of all these curves provides us a model of the "*real*" slit-VS at the reference temperature, denoted by $\mathcal{H}(x)$, minimizing the estimation errors. The modeled slit-VS for a given temperature T can be recovered from $\mathcal{H}(x)$ as:

$$H(x,T) = G_H(T)\mathcal{H}(x - \Delta_x(T)) \tag{4.3}$$

where $\Delta_x(T_0) = 0$ and $G_H(T_0) = 1$. The value for a given pixel column p is obtained integrating the width of the pixel photo-sensible area:

$$H(p,T) = \int_{p-1/2}^{p+1/2} H(x,T)dx \tag{4.4}$$

It is worth noting that Mode 1 performs a binning of columns in pairs. Therefore, for Mode 1 images, we have to simulate the binning in order to obtain the slit-VS factors for each image column:

$$H_1(p_{binned}) = \frac{1}{2}(H_2(p-1) + H_2(p)) \tag{4.5}$$

where $p = \{2, 4, 6, \ldots, 744\}$, and p_{binned} is the pixel number in Mode 1 images (372 columns).

Figure 8 shows a segment of the slit-VS curves modeled independently from Mode 1 and Mode 2 acquisitions $\mathcal{H}_1(x)$ and $\mathcal{H}_2(x)$ (Fig. 8a) and the scatterplot of Mode 1 vs. Mode 2 (Fig. 8b). Agreement between both results is excellent, except in the highest and lowest anomalous values (VS peaks) where probably the interpolation used to obtain $H(x)$ produces underestimated VS peaks, being this effect more noticeable in the binned Mode 1.

Therefore, an optional correction of the vertical striping due to the entrance slit can be performed before the vertical striping removal explained in previous sections.

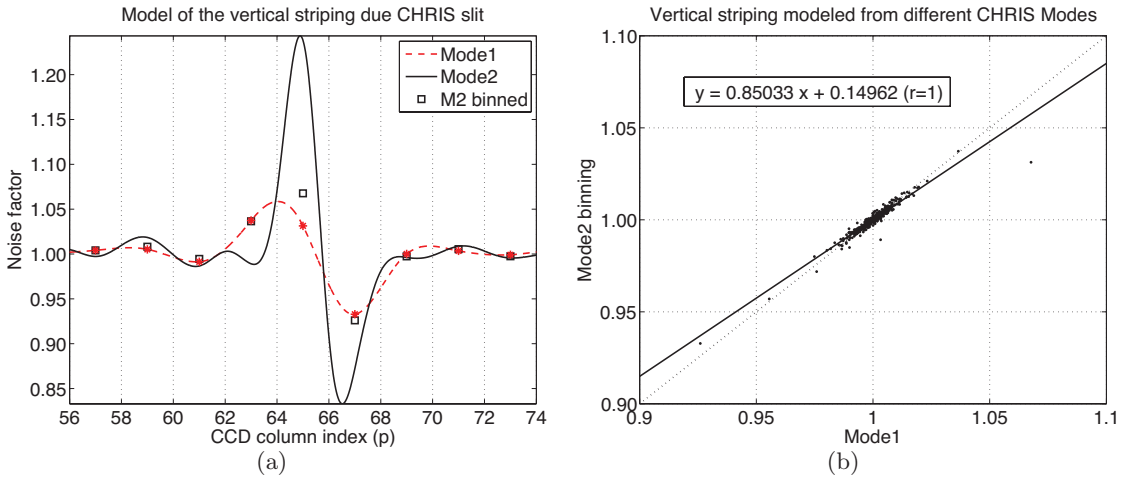

Figure 8: Detail of the "real" slit-VS $\mathcal{H}$ modeled from Mode 1 and Mode 2 CHRIS images, and the binning of Mode 2 '$*$' closely matching Mode 1 curve. Scatterplot of the modeled Mode 1 and Mode 2 "real" slit-VS.

4.4 Algorithm Implementation in the BEAM Toolbox

The correction algorithm proposed in this document has been implemented in the free BEAM Toolbox[2] software in the frame of the ESA project "Development of CHRIS/PROBA Modules for the BEAM Toolbox" (a preview of the noise reduction module is included since BEAM version 4.1).

The approach followed in this project takes advantage of the results presented in previous sections. First, all drop-outs are corrected. Then, a rough correction of the vertical striping due to the entrance slit is performed. For a given CHRIS image, the estimation of the slit vertical striping $H(p,T)$ is obtained from the characterization of the vertical striping pattern $\mathcal{H}(x)$ stored in a look-up-table (LUT) by using Eq. (4.3) to include the dependence on the platform temperature T at the given CHRIS acquisition, and then Eq. (4.4) if the acquisition mode is binned. In Eq. (4.3), we assume a linear dependence of the shift in columns and the gain factor with the temperature: $\Delta_x(T) = -0.12T + 0.65$ and $G_H(T) = 0.13T + 0.28$, respectively, where the coefficients of the linear regression are obtained directly from Mode 2 data presented in Fig. 7. After this preliminary correction of the vertical striping due to the entrance slit, the robust vertical striping correction method proposed in section 4.2 is used to estimate directly from the image (or multiangular acquisition) the remaining vertical striping for each band $\hat{\nu}(p,b)$. Finally, obtained factors are used to correct the image column values .

Figure 9 shows an screenshot of the ESA BEAM Toolbox software. In this example we display the same area for the original CHRIS product (*top*), the image corrected with the algorithm imple-

[2]The Basic ERS & ENVISAT (A)ATSR and MERIS (BEAM) Toolbox (Fomferra and Brockmann, 2005) is a collection of executable tools developed by ESA to facilitate the utilization, viewing, and processing of ESA Earth observation data (http://envisat.esa.int/resources/softwaretools/ or http://www.brockmann-consult.de/beam/).

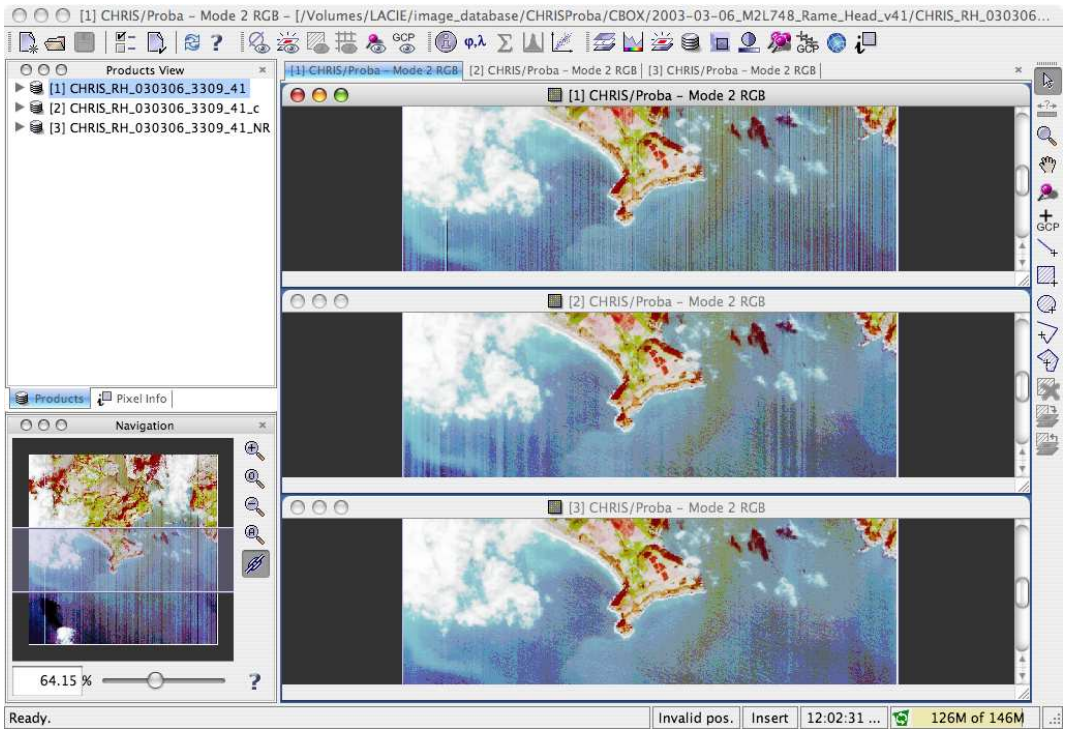

Figure 9: Screenshot with an example of the CHRIS/PROBA noise reduction module implemented in the ESA BEAM Toolbox software.

mented in Settle and Cutter (2005) (*middle*), and the image processed with the CHRIS/PROBA noise reduction module proposed in this document and implemented in the BEAM Toolbox (*bottom*). One can easily appreciate how the vertical patterns are reduced from top to bottom pictures.

5 Conclusions

In this document, several modules that face the problem of removing coherent noises, known as drop-out and vertical striping, usually found in hyperspectral images acquired by push-broom sensors such as CHRIS are presented: (*i*) anomalous odd pixels in image rows due to errors in the transmission of channel 2 (drop-outs), and (*ii*) multiplicative noise in image columns due to irregularities of the entrance slit and CCD elements in the across-track direction (vertical striping). First, pixels presenting drop-outs are detected and corrected by making use of both spatial and spectral information of the drop-out pixel and its neighbours. Although it is a cosmetic correction, it is needed since later processing stages are drastically affected by these anomalous pixel values. Then, the vertical striping pattern is reduced using a new algorithm robust to surface changes. Some algorithms already exist to reduce VS using simple approaches, but they assume that the imaged surface does not contain structures with spatial frequencies of the same order than noise, which is not always the case. The proposed method introduces a way to exclude the contribution of the spatial high frequencies of the surface from the process of noise removal that is based on

the information contained in the spectral domain.

In addition, the proposed algorithm provides a more robust performance in different types of scenes, especially those with sharp transitions between contrasting surfaces; and greater stability of results in the sets of images within an acquisition. These characteristics have permitted to successfully model the shape of the slit with subpixel resolution, and find a relationship of the sensor temperature with the magnitude and distribution of the vertical striping.

Acknowledgement

The authors wish to thank ESA and the former SIRA Space Group (now part of Surrey Satellite Technology Ltd (SSTL)) for the availability of the images and the assistance provided by Dr. Mike Cutter and Lisa Johns. This work has been done in the frame of the project *Development of CHRIS/PROBA modules for the BEAM toolbox* (ESA ESRIN Contract No. 20442/07/I-LG).

Bibliography

Aiazzi, B., Alparone, L., Barducci, A., Baronti, S., and Pippi, I. (2002). Estimating noise and information for multispectral imagery. *Optical Engineering*, 41:656–668.

Barducci, A., Guzzi, D., Marcoionni, P., and Pippi, I. (2005). CHRIS-PROBA performance evaluation: Signal-to-noise ratio, instrument efficiency and data quality from acquisitions over San Rossore (Italy) test site. In *3rd CHRIS/Proba Workshop*, ESRIN, Frascati, Italy. ESA-SP-593.

Barducci, A. and Pippi, I. (2001). Analysis and rejection of systematic disturbances in hyperspectral remotely sensed images of the Earth. *Applied Optics*, 40(9):1464–1477.

Barnsley, M., Settle, J., Cutter, M., Lobb, D., and Teston, F. (2004). The PROBA/CHRIS mission: a low-cost smallsat for hyperspectral, multi-angle, observations of the Earth surface and atmosphere. *IEEE Transactions on Geoscience and Remote Sensing*, 42(7):1512–1520.

Bernaerts, D., Teston, F., and Bermyn, J. (2000). PROBA (Project for Onboard Autonomy). In *5th International Symposium on Systems and Services for Small Satellites*, volume 1, La Baule, France.

Cutter, M. (2004). Review of aspects associated with the CHRIS calibration. In *2nd CHRIS/Proba Workshop*, ESRIN, Frascati, Italy. ESA SP-578, ESA Publications Division.

Cutter, M. and Johns, L. (2005a). CHRIS data format. Technical Report issue 4.2, SIRA - European Space Agency.

Cutter, M. and Johns, L. (2005b). CHRIS data products – latest issue. In *3rd CHRIS/Proba Workshop*, ESRIN, Frascati, Italy. ESA-SP-593.

Fomferra, N. and Brockmann, C. (2005). Beam - the ENVISAT MERIS and AATSR Toolbox. In *MERIS (A)ATSR Workshop 2005*, ESRIN, Frascati, Italy. ESA SP-597, ESA Publications Division.

Garcia, J. and Moreno, J. (2004). Removal of noises in CHRIS/Proba images: Application to the SPARC campaign data. In *2nd CHRIS/Proba Workshop*, ESRIN, Frascati, Italy. ESA SP-578, ESA Publications Division.

Guanter, L., Alonso, L., and Moreno, J. (2005). A method for the surface reflectance retrieval from PROBA/CHRIS data over land: application to ESA SPARC campaigns. *IEEE Transactions on Geoscience and Remote Sensing*, 43(12):2908–2917.

Guanter, L., Estelles, V., and Moreno, J. (2007). Spectral calibration and atmospheric correction of ultra-fine spectral and spatial resolution remote sensing data. Application to CASI-1500 data. *Remote Sensing of Environment*, 109(1):54–65.

Keshava, N. (2004). Distance metrics and band selection in hyperspectral processing with applications to material identification and spectral libraries. *IEEE Transactions on Geoscience and Remote Sensing*, 42(7):1552–1565.

Larsen, R., Nielsen, A. A., and Conradsen, K. (1997). Restoration of hyperspectral push-broom scanner data. In Gudmandsen, P., editor, *Proceedings of the 17th EARSeL Symposium on Future Trends in Remote Sensing*, pages 157–162.

Mlsna, P. and Becker, T. (2006). Striping artifact reduction in lunar orbiter mosaic images. In *IEEE Southwest Symposium on Image Analysis and Interpretation*, pages 95–99.

Mouroulis, P., Green, R. O., and Chrien, T. G. (2000). Design of pushbroom imaging spectrometers for optimum recovery of spectroscopic and spatial information. *Applied Optics*, 39:2210–2220.

Othman, H. and Qian, S.-E. (2006). Noise reduction of hyperspectral imagery using hybrid spatial-spectral derivative-domain wavelet shrinkage. *IEEE Transactions on Geoscience and Remote Sensing*, 44(2):397–408.

Pratt, W. K. (2001). *Digital Image Processing: PIKS Inside, 3rd Edition*. John Wiley & Sons, Inc, New York.

Settle, J. and Cutter, M. (2005). Hdfclean v2: A program for reprocessing images captured by the chris hyper-spectral imager (http://earth.esa.int/proba/).

Theuwissen, A. (1995). *Solid-State Imaging with Charge-Coupled Devices*. Kluwer Acad. Publ., Boston.

Wettle, M., E., B. V., and Dekker, A. G. (2004). A methodology for retrieval of environmental noise equivalent spectra applied to four Hyperion scenes of the same tropical coral reef. *Remote Sensing of Environment*, 93(1-2):188–197.